JOURNAL OF GEOPHYSICAL RESEARCH, VOL. 106, NO. D18, PAGES 20,821–20,831, SEPTEMBER 27, 2001

Lidar measurements during Aerosols99

Kenneth J. Voss,[1] Ellsworth J. Welton,[2] Patricia K. Quinn,[3,4]
James Johnson,[3,4] Anne M. Thompson,[5] and Howard R. Gordon[1]

Abstract. The Aerosols99 cruise (January 14 to February 8, 1999) went between Norfolk, Virginia, and Cape Town, South Africa. A Micropulse lidar system was used almost continually during this cruise to profile the aerosol vertical structure. Inversions of this data illustrated a varying vertical structure depending on the dominant air mass. In clean maritime aerosols in the Northern and Southern Hemispheres the aerosols were capped at 1 km. When a dust event from Africa was encountered, the aerosol extinction increased its maximum height to above 2 km. During a period in which the air mass was dominated by biomass burning from southern Africa, the aerosol layer extended to 4 km. Comparisons of the aerosol optical depth (AOD) derived from lidar inversion and surface Sun photometers showed an agreement within ± 0.05 RMS. Similar comparisons between the extinction measured with a nephelometer and particle soot absorption photometer (at 19 m altitude) and the lowest lidar measurement (75 m) showed good agreement (± 0.014 km^{-1}). The lidar underestimated surface extinction during periods when an elevated aerosol layer (total AOD > 0.10) was present over a relatively clean (aerosol extinction $<$ 0.05 km^{-1}) surface layer, but otherwise gave accurate results.

1. Introduction

The Aerosols99 cruise took place during the period from January 14 to February 8, 1999, on the R/V *Ron Brown*. The cruise track was almost a straight line from Norfolk, Virginia, to Cape Town, South Africa, and afforded the opportunity to sample several different aerosol regimes over the North and South Atlantic. A multidisciplinary group participated on this cruise allowing for the measurement of an extensive suite of chemical, physical, and optical properties of the surface aerosol [*Bates et al*., this issue]. Along with these surface measurements a Micropulse lidar system (MPL) (SESI, Burtonsville, Maryland [*Spinhirne et al*., 1995]) was operated continually, except for brief (1–2 hour) periods around solar noon, to provide vertical profile information on the aerosol distribution. Radiosondes and ozonesondes provided profiles of the temperature, humidity, and ozone distribution, which gave additional information on the structure of the atmosphere. Five-day meteorological back trajectories provided information on the sources of the sampled aerosols. All of this information, when combined, gives additional information on the aerosol structure over the Atlantic.

The cruise track presented a chance to look at many of the aerosol regimes over the Atlantic. This cruise track was impacted by aerosols from the North American continent, by Saharan dust, by biomass burning on the African continent, and by clean maritime air in the regions between. There is very little information on the vertical distribution of the aerosols over the ocean, yet the vertical distribution of these aerosols can impact the accuracy of climate models and atmospheric corrections needed for retrieving ocean color. The Saharan dust and biomass burning aerosols typically absorb light. While atmospheric correction of ocean color imaging can be done for nonabsorbing aerosols without knowledge of the aerosol vertical structure [*Gordon*, 1997], the optical effect of absorbing aerosols is very dependent on the vertical structure [*Gordon et al*., 1997]. Aerosol models for atmospheric correction of ocean color imagery must account for this vertical structure when dealing with absorbing aerosols, yet there are little data available on this problem. This cruise offered an excellent opportunity to measure the aerosol vertical structure and have an extensive set of correlated measurements of the boundary layer aerosol.

In addition to atmospheric correction, it is important to have information on the vertical structure to understand how the surface measurements of the aerosol properties may be related to the total column aerosol properties. During this cruise the MPL was used. This lidar is a very compact system, and with careful calibration and data reduction, accurate information on the aerosol vertical structure of the atmosphere can be obtained. The lidar provides information that can be used to show the presence, or absence, of other layers above the surface boundary layer.

2. Methods

2.1. LIDAR

The MPL averages high-repetition, low-energy pulses to obtain a profile of attenuated backscatter in the atmosphere. The MPL operated at 523 nm, with a pulse repetition rate of 2500 Hz, and the vertical resolution was 75 m. During the day the signal above 10 km became increasingly noisy due to a combination of attenuation in the boundary layer and background sunlight at 523 nm, but during the night low noise data could

[1]Department of Physics, University of Miami, Miami, Florida, USA.
[2]Goddard Earth Science and Technology Center, University of Maryland Baltimore County, Baltimore, Maryland, USA.
[3]Pacific Marine Environmental Laboratory, NOAA, Seattle, Washington, USA.
[4]Joint Institute for the Study of Atmosphere and Ocean, University of Washington, Seattle, Washington, USA.
[5]Atmospheric Chemistry and Dynamics Branch, NASA Goddard Space Flight Center, Greenbelt, Maryland, USA.

Paper number 2001JD900217.
0148-0227/01/2001JD900217$09.00

be obtained to 20 km in the absence of clouds. The details of the algorithm to retrieve the aerosol optical depth (AOD) and vertical profile of extinction or backscattering from the MPL are presented elsewhere [*Welton*, 1998; E. J. Welton et al., Aerosol and cloud measurements using micropulse LIDAR systems, submitted to *Journal of Atmospheric and Oceanic Technology*, 2000, hereinafter referred to as Welton et al., submitted manuscript, 2000]; however, an overview of the technique will be presented here.

The basic equation governing lidar propagation, when the lidar is vertically oriented, is

$$P(z) = CEo(\beta_r(180, z) + \beta_a(180, z)) \cdot \exp\left(-2 \int_0^z [cr(z') + ca(z')]\, dz'\right)/z^2, \quad (1)$$

where $P(z)$ is the received power in a given altitude bin, Eo is the outgoing pulse energy, $\beta_r(180, z)$ is the Rayleigh (molecular) backscattering, $\beta_a(180, z)$ is the aerosol backscattering, c_r is the Rayleigh extinction coefficient, c_a is the aerosol extinction coefficient, and C is an instrument calibration constant. The time the signal is received is related to the altitude z by the time it takes for the lidar pulse to travel up to that altitude and back ($z = tc/2$, where c is the speed of light). By using time-resolved return signals, profiles of the attenuated backscatter can be obtained. While in principle C could be calculated from laboratory measurements [*Spinhirne et al.*, 1980], in practice it is much simpler to derive C from measurements in the field. For a practical lidar system such as the MPL, overlap and afterpulse effects must be taken into account. The overlap function describes the loss in signal strength due to the optical design in the near field. Signals at ranges greater than the overlap range are not effected by this problem. The afterpulse function is a result of cross talk between the laser pulse and detector, as well as detector dark noise in the system (background signal measured even with the system in the dark). Both of these effects were corrected in this data set as described by Welton et al. (submitted manuscript, 2000). Briefly, the overlap function is determined from horizontal lidar measurements of a horizontally homogeneous atmosphere. The deviation from the expected attenuated backscatter return and the actual signal is a measurement of the overlap function. The afterpulse function is determined by running the lidar in a darkened laboratory and blocking the lidar beam at 20 m. The afterpulse function is the apparent signal return.

When the AOD is known from independent measurements (such as with a handheld Sun photometer), the system calibration constant C can be determined (Welton et al., submitted manuscript, 2000). During cloud-free periods during the cruise, episodic measurements of the AOD were made with a Microtops Sun photometer (Solar Light Co., Philadelphia, Pennsylvania). For each lidar profile corresponding to a calibration AOD measurement, a clean aerosol-free layer above the boundary layer was found (for this cruise this was typically 6–7 km). This is usually obvious from the range corrected lidar signal by looking for a layer for which $\ln [P(z)\, z^2]$ is decaying at the rate appropriate for Rayleigh scattering, and typically agrees with a Rayleigh return to within a few percent. The returned power from the aerosol-free layer is simply

$$P(z) = CEo\beta_r(180, z) \cdot \exp\left(-2 \int_0^z [c_r(z') + c_a(z')]\, dz'\right)/z^2 \quad (2)$$

or

$$C = P(z)z^2[Eo\beta_r(180, z) \cdot \exp(-2\ \mathrm{AOD}) \exp\left(-2 \int_0^z c_r(z')\, dz'\right)]^{-1}. \quad (3)$$

All of the factors on the right-hand side of (3) are measured (AOD, E_o, z, and P) or calculated from standard atmosphere profiles (c_r, β_r). Density profiles for standard tropical, winter/summer midlatitude, and winter/summer arctic atmospheres were used as compiled by *McClatchey et al.* [1978] from the U.S. Standard Atmosphere of 1962 and the Supplemental Atmospheres. The density profiles were then used to calculate Rayleigh backscatter and extinction profiles [*Measures*, 1984] for each standard atmosphere. With these factors, C can be determined. Measurements of C were performed throughout the cruise, and C was found to decrease linearly during the cruise by 20%. While we are not sure of the true cause of this variation, variations in the performance of the diode laser, transmission of the optical surfaces, and other factors can influence C. (Note that the lidar detector failed catastrophically on the last day of the cruise so we were not able to determine the true cause of the variation of C after the cruise.) The time variation of the calibration coefficient derived at intervals through the cruise was fit to a linear equation. The accuracy of our calibration procedure is estimated to be ±3%. The calibration uncertainty can be estimated by making seeing how well the calibration curve fits the calibration points obtained during the cruise. The accuracy of the AOD calculation is affected by this calibration coefficient, the accuracy with which the overlap and afterpulse corrections were made, and signal uncertainties. The overlap error is estimated by looking at the deviation of the individual profiles that made up the overlap correction. One example of how the signal uncertainties can increase is when operating near solar noon. Here the background counts are much larger, causing more difficulty in determining the lidar signal. When the AOD is calculated, all these error sources are combined to determine the accuracy of the AOD calculation (Welton et al., submitted manuscript, 2000).

Once the lidar calibration coefficient is determined, the lidar data for the rest of the cruise can be reduced. For each cloud-free lidar profile a clean aerosol-free layer above the boundary layer is found. With the calibration coefficient and this clean layer the returned power is given by (2) above, and (3) can be rewritten to obtain the AOD. It is important to note that this product does not depend on any assumption of the extinction/backscatter ratio.

With the AOD determined, an inversion must be made of the lidar return signal to obtain the extinction or backscattering profile. Since the lidar return depends on both the backscattering and extinction of the aerosols and molecules, this leads to four variables to find from one input. The molecular (Rayleigh) backscatter and extinction coefficients can be calculated, reducing the unknowns. To reduce the number of free variables, an assumption is made about the ratio between the

extinction and backscatter coefficient, otherwise known as S (units are sr). We use an inversion based on *Fernald* [1984] that uses a constant S for aerosols, but have implemented an iterative procedure based on *Marenco et al*. [1997]. Our exact method is described in detail by *Welton* [1998] and Welton et al. (submitted manuscript, 2000). In this method the lidar equation is rewritten in the form

$$P(z) = CEo(\beta_r(180, z) + \beta_a(180, z)) \cdot \exp(-2) \int_0^z [cr(z') + \beta_a(180, z')S_a]\, dz')/z^2, \quad (4)$$

where S_a is S for aerosols. An inversion of the lidar return signal is performed, with an initial guess for S_a, to determine the profile of $\beta_a(z)$. A new estimate of S_a is found by dividing the AOD by the integral of the $\beta_a(z)$ profile. S_a is adjusted with this result, and the procedure is iterated. This process is continued until the change in S_a is less than 0.5%. Since S_a is assumed to be constant, $c_a(z)$ is just $\beta_a(180, z)S_a$.

The final accuracy of this inversion depends on the assumption of a constant S_a through the aerosol layer, and on the errors of the individual corrections (overlap, afterpulse). Even without changes in aerosol composition, changes in RH can effect S_a by changing the size distribution and index of refraction of the aerosols. *Ackermann* [1998] performed a numerical study of the effect of relative humidity on S_a for several aerosol types. The physical properties of the aerosol were taken from *Hess et al*. [1998], and variations on the mixing between hygroscopic and nonhygroscopic aerosols were done. The S_a was calculated from this mix of particle types using Mie theory [*Bohren and Huffman*, 1983], and Ackermann then determined a functional relationship between the RH and S_a for several aerosol regions (continental, maritime, and desert). The cruise radiosonde data indicated that the variation in RH through the aerosol layer changed between the different regions along the cruise track. We will discuss the variation in S_a that might be expected with the RH variation during the discussions of the individual regions.

The constant S_a that is determined from the lidar inversion is a column averaged S_a and may vary between layers, introducing an error into the extinction profile. S_a has been measured to be in the range of approximately 20 sr to 70 sr [*Doherty et al*., 1999]. Thus, for layers which are not a large portion of the total column backscattering, the extinction error may be as large as a factor of 4. The backscatter profile, which is also a product of the inversion algorithm, is much less sensitive to the value of S_a. One can obtain this profile from the extinction profiles presented below by dividing the extinction profile by the S_a found for that particular profile by the inversion. In this paper we present the extinction data because we can compare this inversion result with independent measurements of the surface extinction measured with a nephelometer and a particle soot absorption photometer (PSAP, Radiance Research).

The error estimate for the parameters derived in the inversion (backscattering, extinction) includes the estimated error in the correction functions (overlap and afterpulse), the errors in the AOD value used in the inversion, and are calculated by propagating these error sources through the algorithm.

2.2. Radiosonde

Radiosondes (Vaisala, RS80-15GH) were launched from the deck of the ship at 1045 and 2245 UTC each day. This launch time ensured that each radiosonde would be in the middle of its profile during the synoptic times of 0000 and 1200 UTC. The radiosondes measured vertical profiles of temperature, relative humidity, and horizontal winds. The winds were calculated from GPS measurements of the sonde horizontal position. Most radiosonde profiles extended to at least 15 km altitude. The sondes transmitted one data point every 10 s so that the raw data from the sondes (used here) had a vertical resolution of 20 to 40 m.

To help define the variation of temperature with altitude, the rate of change of the temperature with altitude, $\Delta T/\Delta z$, was derived from the temperature data. $\Delta T/\Delta z$ (°C km^{-1}) was calculated by using a sliding five point least squares-fit to the temperature data (± 2 points around the specific altitude). This altitude interval is approximately 100–200 m.

2.3. Back Trajectories

Five-day back trajectories were made using the isentropic trajectory model at NASA Goddard Space Flight Center [*Schoeberl et al*., 1992]. These trajectories were initialized from the position of the ozonesonde launches along the cruise track. Clusters of back trajectories were run from each launch to capture the uncertainties associated with analyzed winds (Numerical Center for Environmental Prediction (NCEP) 2.5° × 2.5°). The 5-day back trajectories are shown in Figures 1 and 2. The trajectories shown correspond to the weighted central point in each cluster at 1 and 4 km levels. Time of trajectory initiation is 1200 UT with crosses marking every 24 hour.

2.4. Aerosol Regions

Aerosol regions were defined for the marine boundary layer (MBL) by surface trace gas concentrations, aerosol chemical and physical properties, and trajectories at the 500 m arrival height [*Bates et al*., this issue]. These regions may be somewhat different than those defined by other methods such as vertical profiles with lidar or ozonesondes [*Thompson et al*., 2000]; however, to maintain consistency with the surface chemistry measurements, these regional definitions are used in this analysis. By combining the surface information, seven separate MBL regions (regions 1–7) were defined on the basis of the chemical signatures: North American air mass (37°N–31°N), Northern Hemisphere clean (31°N–15.5°N), African dust (15.5°N–8°N), mixed dust and biomass burning (8°N–3°N), biomass burning (3°N–5°S), Southern Hemisphere clean (5°S–24.5°S), and South Atlantic temperate marine air mass (24.5°S–33°S). While surface measurements were available for region 1, because of intense clouds during this period no cloud-free lidar measurements were obtained.

3. Results

The first discussion will compare lidar-derived AOD and extinction to AOD and extinction derived from independent measurements. We will then look at the overall lidar cruise data and investigate the results of the lidar and other vertical profile information for specific cruise regions.

3.1. AOD Comparison

Voss et al. [this issue] shows the complete data set of AOD measurements obtained during the cruise, including the lidar

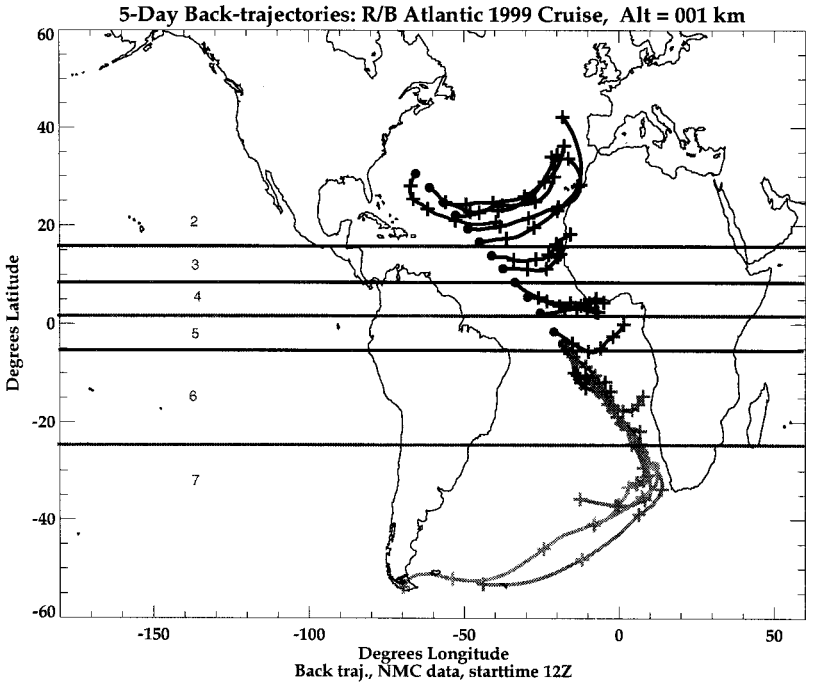

Figure 1. Isentropic back trajectories at 1 km. Aerosol surface chemistry regions are shown divided by lines on the graph. Regions 2–4 have trajectory origins at this altitude on or near the African coast. Regions 6 and 7 indicate South Atlantic clean sources for the surface aerosol.

measurements. This data set included a set of three Microtops Sun photometers independent of the one used to calibrate the lidar. To investigate the agreement between the lidar-derived AOD and the Sun photometer AOD, we grouped the lidar data and Sun photometer data into common 72-min measurement periods. In Figure 3 the comparison between the two data sets are shown for all periods which have measurements with both techniques. The error bars for the Sun photometer measurement is the standard deviation of the distribution of Sun photometer measurements during the specific interval. The lidar error bars are due to the uncertainty in the lidar calibration constant, and signal noise (including afterpulse and

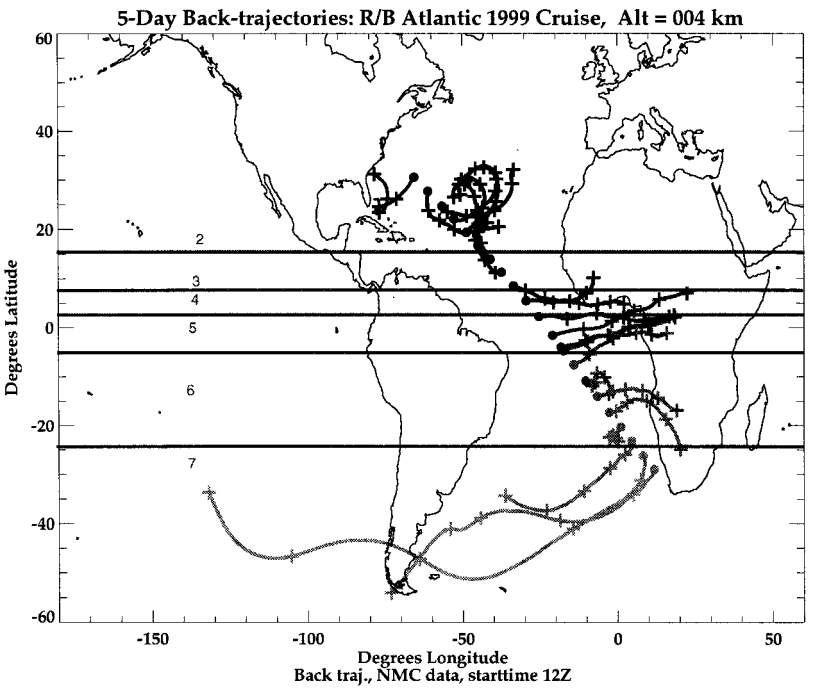

Figure 2. Isentropic back trajectories at 4 km. The elevated trajectories have different origins then the 1 km trajectories (Figure 1). Differences are largest in regions 2 and 3 where the source is the North Atlantic, and region 6 where the elevated trajectory is from the African continent.

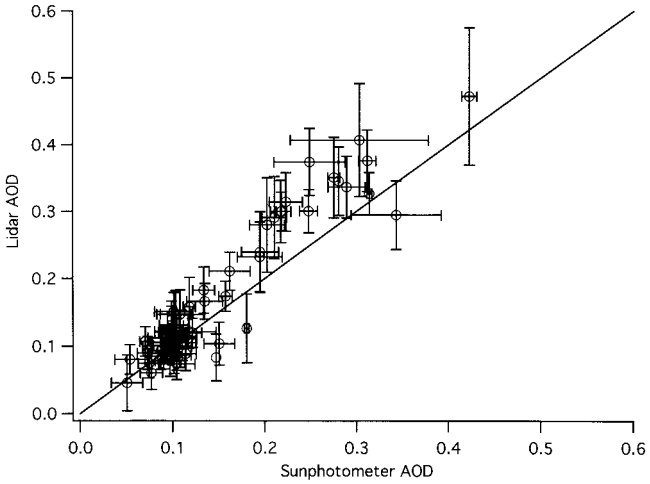

Figure 3. Lidar-derived AOD versus Sun photometer derived AOD for common measurement periods during the cruise. Line is 1:1 fit. Lidar AOD is at 523 nm; Sun photometer AOD ranges from 490 to 500 nm. Error bars on x axis are from the standard deviation of Sun photometer samples common with lidar measurements. Error bars on y axis are from the estimate of the error of the calibration coefficient, and signal noise (including afterpulse and overlap noise).

overlap noise). The line in the figure is the 1:1 line. The agreement between the two methods is good; the RMS difference is 0.05 (optical depth). For larger AOD the lidar AOD appears slightly higher than the Sun photometer AOD. The difference could be due to the lidar technique, to different measurement volumes (the lidar is vertical, the Sun photometer measures along the solar path), a bias in the Sun photometer used for the calibration, or differences in the specific measurement time in the 72 min period. It could also be that in the periods of high AOD either the lidar measurements include very thin clouds, or the Sun photometer measurements are biased by the observer excluding heavier aerosol loads, interpreting them as clouds. Since the AOD is used in the lidar algorithm to determine S_a and the extinction profile, an overestimate of the AOD would tend to overestimate the total column extinction and S_a. In general, though, the lidar derived AOD agrees with the standard Sun photometer technique to within the stated errors.

3.2. Surface Extinction Comparison

We did not have simultaneous measurements of the vertical extinction profile from an independent source (such as an aircraft) during this cruise; however, we have done this in the past and compared this data with the lidar inversion with good results [*Welton et al.*, 2000]. During this cruise we had surface scattering and absorption measurements [*Quinn et al.*, this issue] with which to compare the lowest-altitude bin of the lidar. The aerosol was sampled at 19 m altitude with an integrating nephelometer (TSI Model 3563) and a PSAP. The scattering coefficient (measured at 55% RH and 550 nm) was adjusted to ambient RH using the RH measured on the ship and previously measured f(RH) relationships. For the marine air mass regions, f(RH) for the light scattering coefficient was based on measurements during onshore flow at Cape Grim, Tasmania [*Carrico et al.*, 1998]. In continentally influenced regions, f(RH) from continental air masses at Sable Island, Nova Scotia [*McInnes et al.*, 1998] was used. The Carrico et al.

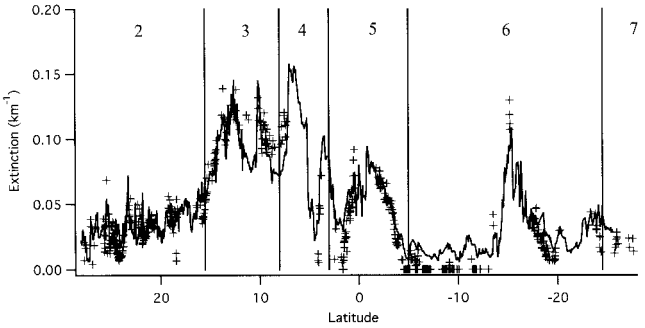

Figure 4. Lidar-derived surface (75 m) extinction (displayed as pluses) and nephelometer surface (19 m) extinction (displayed as the line) throughout the cruise.

f(RH) was used in place of the McInnes et al. marine f(RH) because it was assumed to be more representative of the cleaner Southern Hemisphere marine aerosol; however, the difference between the two was not significant. For the light absorption coefficient (measured at 55% RH and 565 nm), f(RH) was assumed to equal one.

These surface extinction measurements were compared with the extinction retrieved from the lidar inversion at the lowest altitude bin (75 m). The comparison through the cruise is shown in Figure 4. The agreement is generally very good. The RMS difference between the two measurements was 0.014 km^{-1}. However, there are specific regions for which the agreement is not as good. Figure 5 shows the comparison of the two measurements quantitatively. In this figure the measurements are broken into the aerosol regions. The most pronounced bias between the two measurements occurs during portions of region 5 and at the beginning of region 6 (to approximately 13°S). The extreme of this is near 5°–10°S when the surface values of the lidar are set to zero. When there is an elevated aerosol layer, with an AOD > 0.1, above a clean lower layer (extinction < 0.05 km^{-1}), we have found that the lidar inversion underestimates the extinction in the lower layer. Region 2 shows the case where there is a clean lower layer, but the AOD < 0.1. Here the lidar and nephelometer agree well. In regions 3 and 4 at higher surface extinction (extinction > 0.07

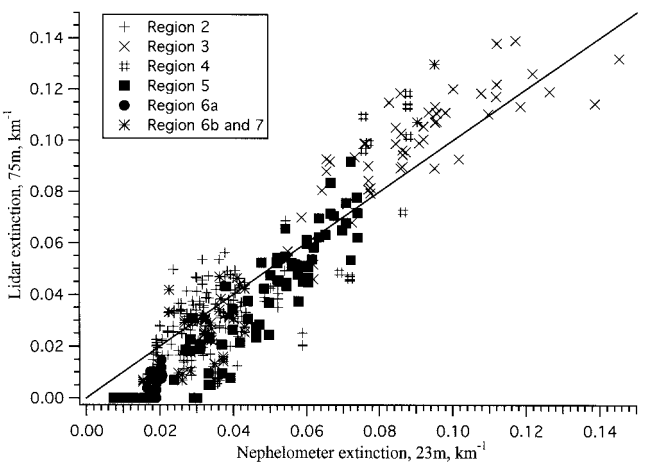

Figure 5. Lidar and nephelometer extinctions during common measurements periods. Measurements are broken into regions as discussed in text. Note the definite regional bias (lidar low) in regions 5 and 6a. Line is 1:1 line for reference.

km^{-1}) there appears to be a 0.01–0.02 km^{-1} bias in the extinction. Two sources could be hypothesized for this bias. First, it could be that the column S_a is an overestimate of the true S_a in this lowest region, hence the bias is due to the constant S_a assumption. The second hypothesis could be that since the lidar profile shows a large increase in the lower portion of the air column (between 75 and 500 m), this bias could be due to the difference in sampling height between the nephelometer and the lowest bin of the lidar. In general, though, the lidar inversion worked well even at this low altitude, which has the most difficulties due to the strong overlap function.

3.3. LIDAR Data Through Cruise

Plate 1a shows the contour plot of the extinction profile during the cruise. The contour plot is built from the lidar data, with 75 m vertical resolution and at the data points marked at the bottom of the graph. Gaps in data were predominately due to clouds; however, during periods of high Sun angle (solar noon) the lidar was turned off to avoid direct sunlight entering the detector (this also had to take into account possible ship roll, as direct sunlight would cause a complete failure of the system). There was a large variation in both vertical structure and magnitude of the extinction, which was dependent on both location and recent meteorological transport.

While the aerosol obviously reached higher levels near the equator, it is also interesting to see how the aerosol is distributed, proportionately, for a given profile. Plate 1b shows a contour of the integrated extinction coefficient. This was calculated as

$$\text{integrated extinction } (z) = \frac{\int_0^z Ca(z')\,dz')}{\int_0^{6\text{ km}} Ca(z')\,dz')} \times 100. \tag{5}$$

The altitude 6 km was used as a reference because we found negligible aerosols above this altitude during this cruise. Once again, the data points on which the contours were produced are shown at the bottom of the graph. Before 8°N and after 15°S, 25 and 50% lines (the altitude at which 25 and 50% of the AOD has been accounted for already) are fairly constant at 0.5 and 0.8 km. The 75 and 90% lines during this time show periods for which more aerosol (relative to the rest of the column) was added at 1–1.5 km (approximately 14°N and 20°S). Between 8°N and 15°S the surface layer (below 500 m) is cleaner than the elevated layers. Thus all the contours rise during this period. In particular, at the beginning of region 6 the 90% level was the highest of the cruise. At this time there was a very clean lower level, and an elevated aerosol. While the optical depth [*Voss et al*., this issue] and extinction (Plate 1) were not maximum here, the clean lower level had the effect of making the upper aerosols a more important contribution to the column properties.

Figure 6 shows S_a derived from the lidar inversions through the cruise; also shown are the error bars on this derived parameter (method described by Welton et al., submitted manuscript, 2000). Errors are estimated by propagating the uncertainties in the overlap correction, afterpulse correction, background signal, calibration coefficient, and AOD through the inversion algorithm. The S_a will also be discussed in the specific regional discussions below, but the main feature is that during the periods of low total column extinction and low AOD, in regions 2 and late 6, S_a tended to have low values characteristic of maritime aerosols. During the periods of high AOD and high total column extinction, S_a was higher, typical of smaller particles and continental aerosols.

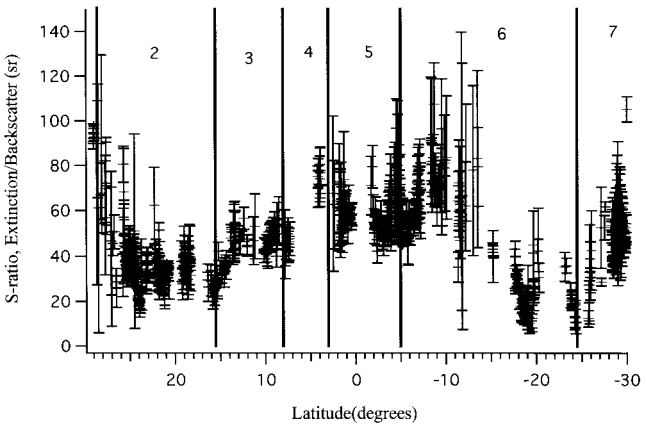

Figure 6. S_a (extinction/backscattering) derived throughout the cruise. Vertical lines delineate regions. S_a was lower in clean maritime air masses then in those impacted by dust or biomass burning.

3.4. Specific Regional Vertical Structure Features

We will now discuss the differences in vertical structure of the lower atmosphere (<7 km) defined for the different regions. For each region a typical radiosonde/lidar profile is shown. In each case the figure shows the radiosonde data (RH and $\Delta T/\Delta z$) along with the average of three lidar extinction coefficient profiles obtained within 1 hour of the radiosonde profile. The error bars on the lidar profiles are a combination of the estimated error in the inversion (calibration coefficient, overlap function and afterpulse function) combined with the standard deviation of the three profiles combined to make this average. As discussed previously, because of our assumption of a constant S_a, the extinction profile is subject to larger errors than the backscatter profile. The backscatter profile can be obtained from our extinction profile by a simple multiplication by $1/S_a$. We prefer to discuss the profile in terms of extinction, however, as we have the surface validation discussed in section 3.2.

One common feature in all of our lidar profiles is an increase in extinction from the surface to an altitude between 500 and 1000 m, below the top of the boundary layer. This does not follow the normal idea of a well-mixed boundary layer; however, this behavior has been reported previously in the tropical maritime atmosphere [*Sasano and Browell*, 1989]. Similar features were also seen during the TARFOX experiment over the North Atlantic, when haze plumes advected from the North American continent [*Ismail et al*., 2000]. The reason for this structure in our experiment is not understood. Because of intense clouds, there are no lidar data for region 1, so we begin our discussion with region 2.

3.4.1. Region 2: Northern Hemisphere clean (31°N–15.5°N). In this region, back trajectories at 1 and 4 km indicated that the air mass origin was over the North Atlantic (Figures 1 and 2). Surface measurements of the aerosol chem-

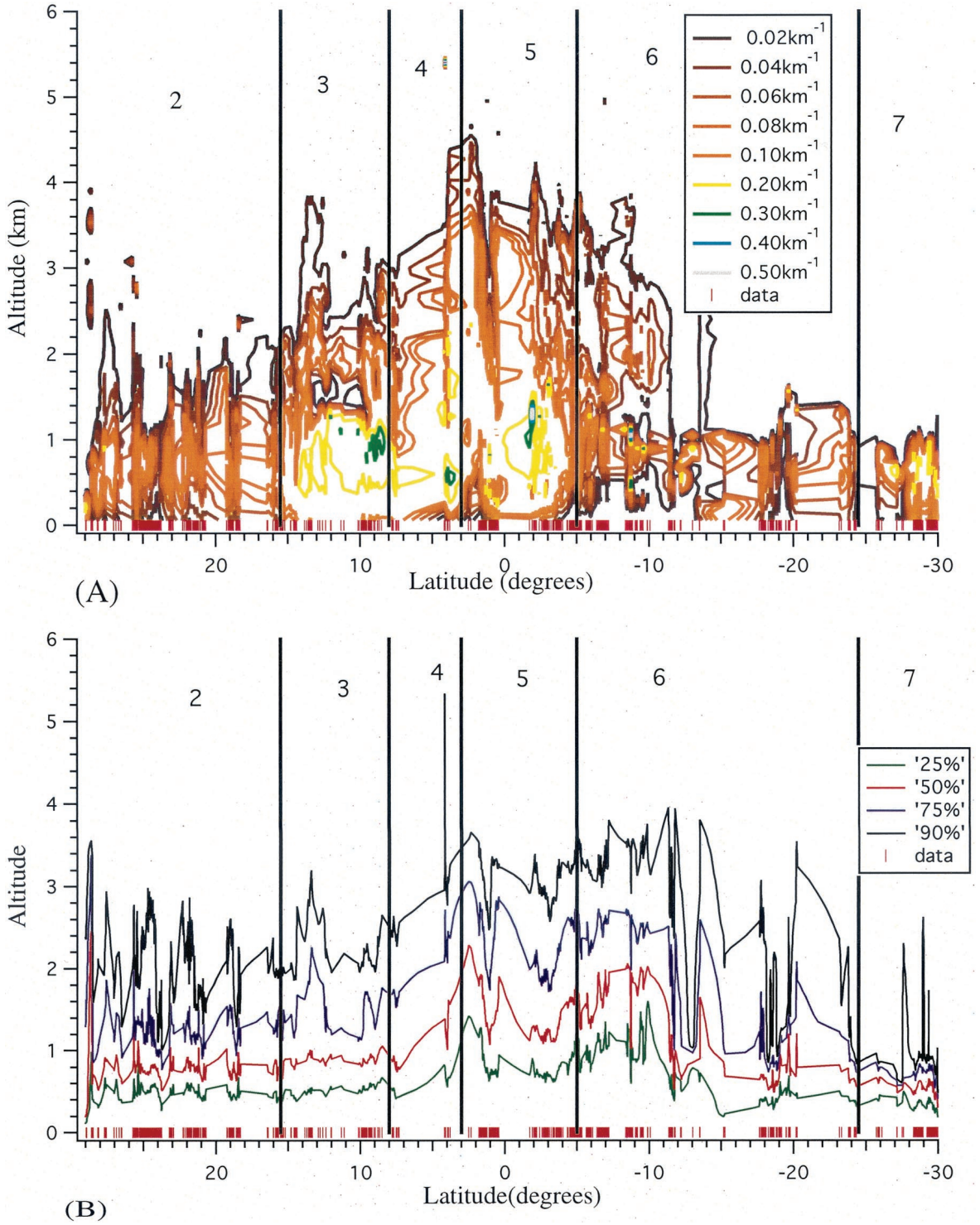

Plate 1. Contour plot of (a) lidar-derived extinction coefficients and (b) integrated extinction from the surface to altitude z, along the cruise track. Regions are delineated by the lines. The data positions on which the contours are based are shown as lines at the bottom of the graph.

istry indicated that the aerosol was clean maritime aerosol [*Bates et al*., this issue].

Example radiosonde and lidar profiles from this region (for DOY 18.5, 27.7°N) are shown in Figure 7. In the example shown, there is a strong temperature inversion at 1 km, and another at 2 and 4.5 km. The RH, in this example, stayed relatively constant at 80 ± 10% up to 3 km. The aerosol was capped by the 1 km inversion, as witnessed by the lidar extinction coefficient.

In general, in this region, the extinction coefficient was low (less than 0.2 km^{-1} peak), and the peak extinction coefficient was below 1 km, with very little extinction above 1 km (the example in Figure 8 had the largest extinction above 1 km in region 2). The extinction profiles indicated that 90% of the

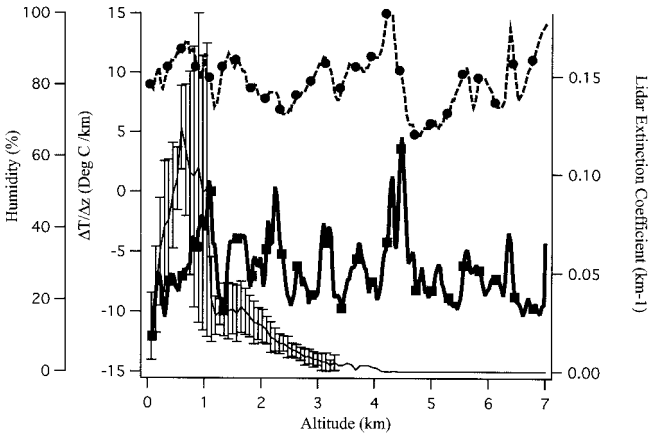

Figure 7. Radiosonde and lidar-derived profiles typical for region 2, Northern Hemisphere clean (31°N–15.5°N). This specific case was for DOY 18.5, 27.7°N. LIDAR extinction is shown as the fine line with no symbols. This is an average of the nearest three profiles (each of which is a 10 min cloud-free average) around the radiosonde launch. Relative humidity is displayed as the dashed line marked with solid circles, while $\Delta T/\Delta z$ is displayed as the line marked with solid squares. Note overall extinction is low and capped by the first temperature inversion (positive $\Delta T/\Delta z$). Error bars on the lidar extinction combine error estimate due to calibration uncertainties with the standard deviation of the three profiles used to make the average.

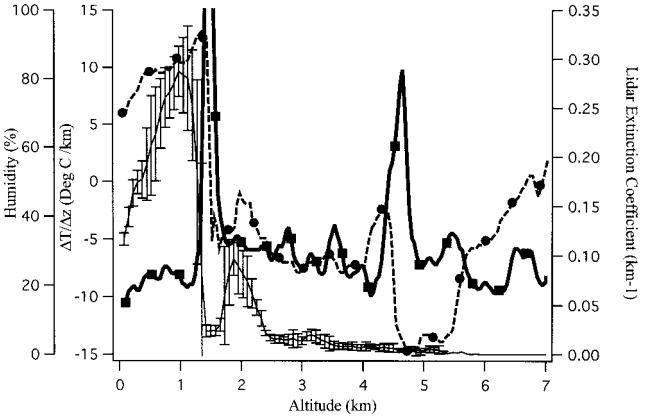

Figure 8. Region 3: dust (15.5°N–8°N). This specific case was for DOY 24.5, 11.2°N. Symbols and error bars are as in Figure 7. Extinction has increased from region 2, and there is another aerosol layer above the first temperature inversion (positive $\Delta T/\Delta z$).

AOD occurred below 2–3 km. The temperature structure seemed to vary, with strong inversions often occurring between 1 and 1.5 km. These temperature inversions were typically associated with the top of the aerosol layer. Relative humidity was generally above 80% throughout the aerosol layer.

Since the surface chemistry and back trajectories all indicated that this was a maritime atmosphere, there is no indication that there were drastic changes in aerosol composition in the aerosol layer. With the RH limited between 80 and 100%, *Ackermann*'s [1998] model for S_a for a maritime atmosphere indicates that the value should be approximately 25 sr, with RH effects only indicating a range from 23–27 sr. Thus our assumption of a constant S_a is a reasonable approximation in this region. We found that the S_a average for this region was 32 ± 6 sr, which is near the values derived by Ackermann. *Doherty et al*. [1999] found S_a to be 21.1 ± 3.7 sr for a maritime aerosol using a direct measurement technique; however, this measurement was at a lower RH (<40%). *Sasano and Browell* [1989] reported an S_a of 30 sr for a maritime aerosol (at 600 nm). As discussed elsewhere [*Voss et al*., this issue], the AOD was low in this region (around 0.09 ± 0.02) with a low angstrom exponent (0.27 ± 0.27). The angstrom exponent α is related to the spectral variation of the AOD [$\mathrm{AOD}(\lambda) = \mathrm{AOD}(\lambda_o)\lambda^{-\alpha}$]. A low angstrom exponent indicates a size distribution weighted toward large particles [*van de Hulst*, 1981], and the low value of S_a also indicates a dominance of large particles [*Doherty et al*., 1999].

One final feature in this region was that initially the RH stayed high (>60%) throughout the column below 7 km. At 25°N the structure changed, becoming dryer above 3 km. By 23.7°N the humidity was less than 10% between 3 and 6 km, with some excursions above 10% occurring between 6 and 7 km. Since this was above the aerosol layer, there was no visible effect on the aerosol vertical structure. A more complete picture of the vertical profile of RH through the cruise is shown by *Bates et al*. [this issue].

3.4.2. Region 3: Dust (15.5°N–8°N). During the next portion of the cruise we had a significant dust event that changed the surface and vertical aerosol structure. Back trajectories at 1 km showed the aerosol source switching to the coast of Africa, with 4 km trajectories still coming from the North Atlantic.

A typical example of the vertical structure is shown in Figure 8 for day 24.5, 11.2°N. The radiosonde data throughout this period indicated a strong temperature inversion at 1.5 km and another temperature feature at 4–5 km. The RH was relatively constant at 80–100% in the lower layer, below the 1.5 km temperature inversion. However, at this inversion the RH decreased rapidly to 40% and continued to decrease to 20%. The RH stayed constant at this level to the upper temperature feature (4–5 km) where it seemed to decrease to near 0% RH for a 1 km layer, after which it would increase back to 20–40%.

The lidar profile data showed two distinct layers, with a sharp minimum in extinction between them. The lower layer was capped by the temperature inversion at 1.5 km. The upper layer peaked at 2 km, with a subsequent gradual decrease with altitude. By 4 km the aerosol extinction was very low (<0.02 km^{-1}). The peak extinction in the lower layer was approximately 0.3 km^{-1}, while the peak extinction in the next layer was approximately 0.1 km^{-1}, so most of the AOD occurred in the lower layer. During this period, 90% of the AOD occurred below 2–3 km.

The column averaged S_a during this period was 41 ± 8 sr. This is significantly higher than the S_a predicted by *Ackermann* [1998] for desert aerosols. Ackermann's work assumed spherical particles; however, dust particles are often nonspherical which increases S_a by decreasing the backscattering at 180°. This value for S_a (41 ± 8 sr) agrees with earlier measurements by *Welton et al*. [2000] (37 ± 9 sr), *Sasano and Browell* [1989] (52 ± 10 sr), and *Rosen et al*. [1997] (41.6 ± 8 sr). In this region, while the RH in each layer was relatively constant, the RH changed significantly between the upper and lower layer (80–100% to 40%). However, because desert aerosol responds only weakly to RH, this change effects S_a very weakly (less than 10% change in S_a [*Ackermann*, 1998]). Thus changes in

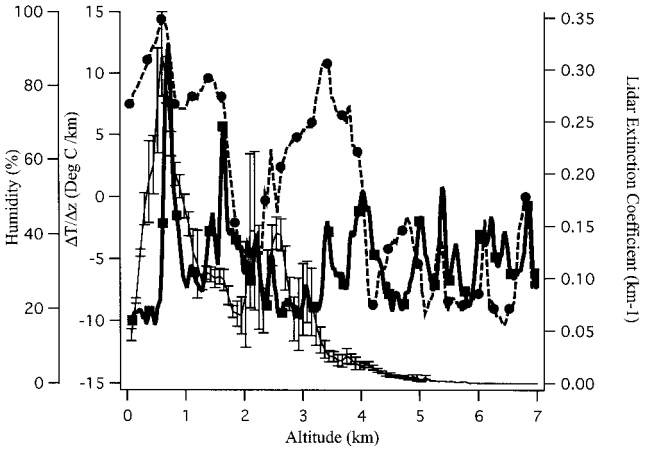

Figure 9. Region 4: mixed dust and biomass (8°N–3°N). This specific case was for DOY 26, 7.5°N. Symbols and error bars are as in Figure 7. Extinction is still high. The temperature, humidity, and aerosol structure are all much more complicated than earlier in the cruise.

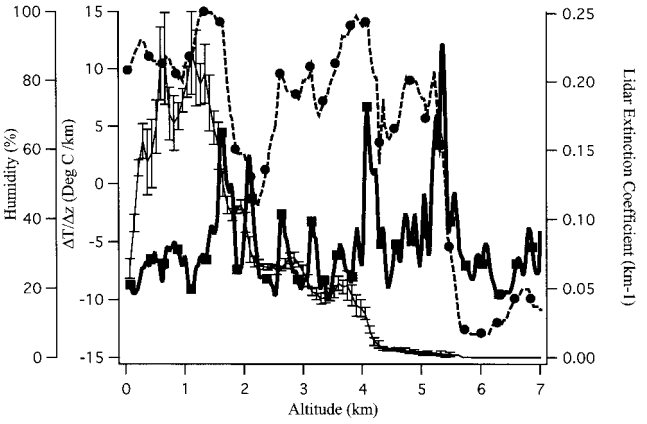

Figure 10. Region 5: biomass burning (3°N–5°S). This specific case was for DOY 29, 2.3°S. Symbols and error bars are as in Figure 7. Extinction is still high. Aerosol layer does not show a minimum between upper and lower layers.

the S_a due to humidity are not expected. With the upper layer being very distinct, it is possible that a different aerosol was in the upper layer. While we have no in situ chemical information on this layer, the air mass trajectories from 4 km indicate a more marine origin for this upper layer. If this is the case, then the S_a we found for the clean maritime case (region 2, averaged 32 ± 6 sr) may be used; however, this is not appreciably different than the S_a used. A cleaner maritime layer above the surface layer would cause our extinction in the lower layer to be very slightly overestimated, while the upper layer may be slightly underestimated. A fit of the nephelometer data to the lidar surface data for this region shows that there is a small (0.02 km^{-1}) overestimate in the surface lidar extinction. However, we still do not feel we have enough information to quantitatively implement a layered S_a algorithm for the lidar inversion.

3.4.3. Region 4: Mixed dust and biomass burning (8°N–3°N). This period was characterized by the surface chemistry to be changing from the previous dust event to a biomass-burning aerosol. Back trajectories at 1 and 4 km indicated that the column aerosol was coming from Africa. Radiosonde data indicated very strong and varying temperature and humidity structure through this period, and it is difficult to pick a representative profile. Figure 9 is an example of the structure during this period, for day 26, 7.5°N. In all of the radiosondes there was a strong temperature inversion near 1 km. At times there were other inversions above this with varying strength. The humidity was typically high (above 80%) below the lower inversion, but in the lower 7 km the RH decreased irregularly to 20–40%.

There was always a large lidar-derived extinction peak near 1 km, with extinction values on the order of 0.3 km^{-1}. Additionally, another peak (near 0.2 km^{-1}) occurred at approximately 2 km. The aerosols continued higher, with significant extinction to near 4 km. The 90% level for the integrated extinction coefficient was at 2.7 km, somewhat higher than in previous regions. The minimum between the lower and upper peak was not as distinct, or at as low an altitude, in this region as in the previous indicating there may have been more mixing between the layers. The average S_a in this region increased to 52 ± 10 sr, which is between Ackermann's continental and desert aerosols, possibly reflecting the mix of aerosols at this location. With the large peaks in aerosol extinction the AOD was significantly higher with the average AOD being 0.41. The angstrom exponent was also higher here, reaching 0.52, but because of clouds there were few Sun photometer measurements on which to base this angstrom exponent.

3.4.4. Region 5: Biomass burning (3°N–5°S). The next region reached during the cruise had surface aerosol chemistry characteristics of biomass burning. Back trajectories at 1 km were mostly over the South Atlantic; however, 4 km trajectories were from central Africa, and the 8 km trajectories were also from the African coast.

Typical radiosonde and lidar data are shown in Figure 10 and are from DOY 29, 2.3°S. In this region there were typically temperature inversions at 1.5–2 km, then other inversions above this (3, 4, 5 km, and above). The RH varied between staying above 80% all the way to 4.5 km, to having a minimum of 40% at 2 km. It is difficult to find a general trend.

The aerosol extinction profile also varied over this region. In all cases, significant aerosol extinction extended to 4 km. The 90% AOD level in this region averaged 3.3 km. The peak extinction reached >0.20 km^{-1}, with broad (>2 km) peaks. At times the peak moved off of the 1 km level to 2–3 km, but was typically at 1 km. The aerosol also seemed to decrease at 2 km, but then maintained a significant extinction to 4 km. The S_a during this period was relatively high, 60 ± 6 sr. We could not find other values of S_a for biomass burning aerosols; however, the S_a for continental aerosols (which would also be absorbing) was similar. Our S_a was a little lower than the value predicted for continental aerosol at this RH (>80%) by *Ackermann* [1998]. *Doherty et al*. [1999] found S_a to vary from 60.4 to 69.9 ± 9.7 sr for continental aerosols, which agrees with our measurement. The average AOD was high, 0.36, with a very high average angstrom exponent of 0.882. This indicates that the aerosol particles were probably relatively small, which agrees with the retrieved S_a.

3.4.5. Region 6: Southern Hemisphere clean (5°S–24.5°S) and region 7: South Atlantic temperate marine air mass (24.5°S–33°S). After going through these intense aerosol events, the surface chemistry again indicated a clean maritime situation [*Bates et al*., this issue]. Interestingly, while the sur-

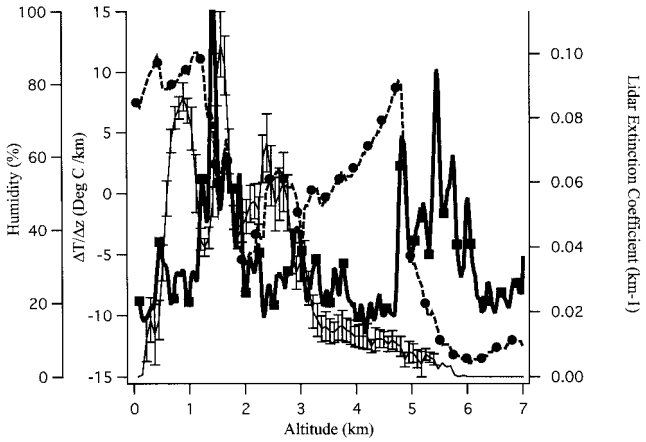

Figure 11. Early portion of region 6: Southern Hemisphere clean (5°S–24.5°S). This specific case was for DOY 30.5, 7.4°S. Symbols and error bars are as in Figure 7. Extinction is still high. This area was distinguished by having low surface extinction with an elevated aerosol layer with high extinction.

face measurements indicated a change at 5°S, the back trajectories did not switch as rapidly. The 1 km trajectories were over the South Atlantic; however, early in the region (between 5°S and 12°S), 4 km trajectories were still over southern Africa and only switched to the South Atlantic after 12°S. An example of the earlier period is shown in Figure 11, while an example of the later period is shown in Figure 12. Figure 11 is for day 30.5, 7.4°S, while Figure 12 is for day 35.5, 23.6°S. We have grouped these two regions together because the vertical structure of the late part of region 6 was basically the same as that of region 7.

The radiosonde data for the earlier period show a strong temperature inversion at 1.5 km. The RH is typically very high (>80%) below this inversion, but decreases at the inversion to 50–60%. The aerosol extinction profile shows why the surface chemistry appeared clean, yet column AOD was not small. One can see that the surface extinction is below 0.01 km^{-1}, while the column extinction reaches >0.09 km^{-1} at 1 km or greater. During this early period, significant aerosol extended

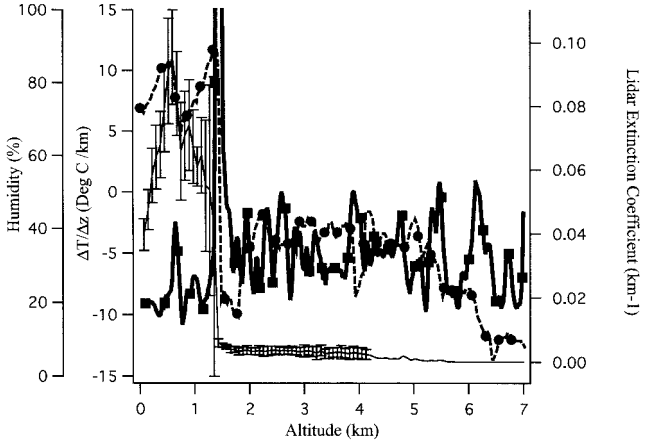

Figure 12. Later portion of region 6: Southern Hemisphere clean (5°S–24.5°S) and region 7: South Atlantic temperate marine air mass (24.5°S–33°S). This specific case was for DOY 35.5, 23.6°S. Symbols and error bars are as in Figure 7. Extinction is now low again. This area is similar to the clean Northern Hemisphere case.

to 4 km, with the average 90% AOD level at 3.2 km, showing how high the aerosol was in the atmospheric column. The S_a in the early period was 63 ± 12 sr, much higher than the values determined for the Northern Hemisphere clean region, and close to the value of the biomass burning. As discussed earlier, the algorithm results are more uncertain when an optically dense upper layer is above a clean maritime layer. The algorithm tends to underestimate the extinction in the lower level. In terms of the overall column optics this is not a significant error.

By the end of the period the region resembles the Northern Hemisphere clean situation (Figure 12). The radiosondes show a strong inversion at approximately 1.5 km. The RH stays high (80–100%) to this altitude then drops to low values (30–40%) above the inversion. Aerosols are capped at 1 km by the inversion, but only reach extinction of 0.1 km^{-1} or so below the inversion and are at background (<0.01 km^{-1}) above the inversion. The 90% integrated extinction level is at 1.4 km. The S_a also decreases to levels seen in the first region (36 ± 16 sr). AOD and angstrom exponents are also down to the values in region 2 (0.094 and 0.35, respectively [*Voss et al.*, this issue]). The structure in these clean Northern and Southern Hemisphere cases is the same.

4. Conclusions

With the lidar and associated measurements during this cruise we were able to determine the aerosol vertical structure of the lower portion (<7 km) of the atmosphere. Comparisons of the lidar-derived AOD and extinction with Sun photometers and a surface nephelometer and PSAP showed that the lidar inversions were giving reasonable results throughout the cruise. A specific situation, when there is a clean lower layer (extinction < 0.05 km^{-1}) below an elevated aerosol layer (AOD > 0.1), caused the near-field lidar inversion to underestimate the surface extinction. However, for the most part, the lidar-derived AOD and extinction agreed within the expected errors.

Lidar inversions to obtain the extinction profile illustrated a varying vertical structure depending on the dominant air mass and on the temperature structure of the atmosphere. In the periods of clean maritime aerosols in the Northern and Southern Hemisphere the aerosols were predominantly below 1–2 km. A dust event from Africa increased the maximum height of aerosol extinction to between 2 and 3 km. During a period in which the air mass was dominated by biomass burning from southern Africa, the aerosol layer extended to 3–4 km.

Ocean color algorithms for this region will have to take into account the extended height of the aerosol column during these dust events. The dust is an absorbing aerosol, and as such an extended height would have the effect of reducing the aerosol reflectance in the absorbing portion of the spectrum (blue region). Hence, without an accurate vertical profile, the atmospheric correction would tend to overcorrect in the blue.

Of course, this data set is a snapshot of the aerosol structure over this region. Extended measurements and more cruises in the area with lidars would be useful to determine how often these conditions exist. However, given the lack of data on this subject in this area, these results give a basis on which to build a better climatology of the aerosol structure in this region.

Acknowledgments. We thank the officers and crew of the NOAA R/V *Ron Brown*. We would like to acknowledge the support of NASA

under contract NAS5-31363 (K.J.V., E.W., and H.R.G.). Part of this work (P.K.Q.) was funded by the Aerosol Program of the NOAA and the NASA Global Aerosol Climatology Project.

References

Ackermann, J., The extinction-to-backscatter ratio of troposphere aerosol: A numerical study, *J. Atmos. Oceanic Technol*., *15*, 1043–1050, 1998.

Bates, T. S., P. K. Quinn, D. J. Coffman, J. E. Johnson, T. L. Miller, D. S. Covert, A. Wiedensohler, S. Leinert, A. Nowak, and C. Neususs, Regional physical and chemical properties of the marine boundary layer aerosol across the Atlantic during Aerosols99: An overview, *J. Geophys. Res*., this issue.

Bohren, C. F., and D. R. Huffman, *Absorption and Scattering of Light by Small Particles*, 530 pp., John Wiley, New York, 1983.

Carrico, C. M., M. J. Rood, and J. A. Ogren, Aerosol light scattering properties at Cape Grim, Tasmania, during the First Aerosol Characterization Experiment (ACE 1), *J. Geophys. Res*., *103*, 16,565–16,574, 1998.

Doherty, S. J., T. L. Anderson, and R. J. Charlson, Measurement of the lidar radio for atmospheric aerosols with a 180 deg backscatter nephelometer, *Appl. Opt*., *38*, 1823–1832, 1999.

Fernald, F. G., Analysis of atmospheric lidar observations: Some comments, *Appl. Opt*., *23*, 652–653, 1984.

Gordon, H. G., Atmospheric correction of ocean color imagery in the Earth Observing System era, *J. Geophys. Res*., *102*, 17,081–17,106, 1997.

Gordon, H. G., T. Du, and T. Zhang, Remote sensing ocean color and aerosol properties: Resolving the issue of aerosol absorption, *Appl. Opt*., *36*, 8670–8684, 1997.

Hess, M., P. Koepke, and I. Schult, Optical properties of Aerosols and Clouds: The software package OPAC, *Bull. Am. Meteorol. Soc*., *79*, 831–844, 1998.

Ismail, S., E. V. Browell, R. A. Ferrare, S. A. Kooi, M. B. Clayton, V. G. Brackett, and P. B. Russell, LASE measurements of aerosol and water vapor profiles during TARFOX, *J. Geophys. Res*., *105*, 9903–9916, 2000.

Marenco, F., V. Santacesaria, A. F. Bais, D. Balis, A. di Sarra, A. Papayannis, and C. Zerefos, Optical properties of tropospheric aerosols determined by lidar and spectrophotometric measurements (Photochemical Activity and Solar Ultraviolet Radiation campaign), *Appl. Opt*., *36*, 6875–6886, 1997.

McClatchey, R. A., R. W. Fenn, J. E. A. Selby, F. E. Volz, and J. S. Garing, Optical properties of the atmosphere, in *Handbook of Optics*, edited by W. G. Driscoll, pp. 14-1–14-65, McGraw-Hill, New York, 1978.

McInnes, L., M. Bergin, J. Ogren, and S. Schwartz, Apportionment of light scattering and hygroscopic growth to aerosol composition, *Geophys. Res. Lett*., *25*, 513–516, 1998.

Measures, R. M., *Laser Remote Sensing Fundamentals and Applications*, 510 pp., John Wiley, New York, 1984.

Quinn, P. K., D. J. Coffman, T. S. Bates, T. L. Miller, J. E. Johnson, K. Voss, E. J. Welton, and C. Neususs, Dominant aerosol chemical components and their contribution to extinction during the Aerosols99 cruise across the Atlantic, *J. Geophys. Res*., this issue.

Rosen, J. M., R. G. Pinnick, and D. M. Garvey, Measurement of extinction-to-backscatter ratio for near-surface aerosols, *J. Geophys. Res*., *102*, 6017–6024, 1997.

Sasano, Y., and E. V. Browell, Light scattering characteristics of various aerosol types derived from multiple wavelength lidar observations, *Appl. Opt*., *28*, 1670–1679, 1989.

Schoeberl, M. R., L. R. Lait, P. A. Newman, and J. E. Rosenfield, The structure of the polar vortex, *J. Geophys. Res*., *97*, 7859–7882, 1992.

Spinhirne, J. D., J. A. Reagan, and B. M. Herman, Vertical distribution of aerosol extinction cross section and inference of aerosol imaginary index in the troposphere by LIDAR technique, *J. Appl. Meteorol*., *19*, 426–438, 1980.

Spinhirne, J. D., J. Rall, and V. S. Scott, Compact eye-safe LIDAR systems, *Rev. Laser Eng*., *23*, 26–32, 1995.

Thompson, A. M., B. G. Doddridge, J. C. Witte, R. D. Hudson, W. T. Luke, J. E. Johnson, B. J. Johnson, S. J. Oltmans, and R. Weller, A tropical Atlantic paradox: Shipboard and satellite views of a tropospheric ozone maximum and wave-one in January–February 1999, *Geophys. Res. Lett*., *27*, 3317–3320, 2000.

van de Hulst, H. C., *Light Scattering by Small Particles*, 470 pp., Dover, Mineola, N. Y., 1981.

Voss, K. J., E. J. Welton, P. K. Quinn, R. Frouin, M. Miller, and R. M. Reynolds, Aerosol optical depth measurements during the Aerosols99 experiment, *J. Geophys. Res*., this issue.

Welton, E. J., Measurements of aerosol optical properties over the ocean using Sunphotometry and LIDAR, 150 pp., Ph.D. dissertation, Univ. of Miami, Coral Gables, Fla., 1998.

Welton, E. J., et al., Ground-based LIDAR measurements of aerosols during ACE-2: Instrument description, results, and comparisons with other ground-based and airborne measurements, *Tellus*, *52*, 635–651, 2000.

H. R. Gordon and K. J. Voss (corresponding author), Department of Physics, University of Miami, Miami, FL 33124, USA. (voss@physics.miami.edu)

J. Johnson and P. K. Quinn, Pacific Marine Environmental Laboratory, NOAA, Seattle, WA 98115, USA.

A. M. Thompson, Atmospheric Chemistry and Dynamics Branch, NASA Goddard Space Flight Center, Greenbelt, MD 20771, USA.

E. J. Welton, Goddard Earth Science and Technology Center, University of Maryland Baltimore County, Baltimore, MD 21250, USA.

(Received July 18, 2000; revised February 2, 2001;
accepted May 10, 2001.)